Numerical Investigation of Buoyancy-Aided Flow in the Rod-to-Wall Gap Regions

Y.Duan[1], S. He[1]*
[1]Department of Mechanical Engineering, University of Sheffield, Sheffield S1 3JD,UK
mep10yd@sheffield.ac.uk; s.he@sheffield.ac.uk

ABSTRACT

The principle objective of this paper is to report a numerical investigation of the buoyancy-aided flow in the non-uniformed geometry by using large-eddy simulation (LES) with a wall-adapting local subgrid scale model. The wall-to-diameter ratio is 1.08. Four cases are studied, one forced convection case and three buoyancy aided convection cases. The Reynolds number based on the hydraulic diameter is Re_D=5270, and the buoyancy parameters *Bo** of the buoyancy influenced cases are $1.5x10^{-6}$, $2.4x10^{-6}$ and $1.7x10^{-5}$, respectively. Fluid properties are assumed to be constant and the buoyancy effect is modelled by using the Boussinesq approximation.

The existence of large flow structures in the narrow gap in all of the considered cases are demonstrated using the instantaneous history of turbulent velocities. It exhibits itself as a swinging flow structure in the narrow gap when the Buoyancy parameter *Bo** is smaller than the critical value Bo_0^*. As the buoyancy force becomes stronger, the characteristics of the flow structure change. The overall buoyancy effect on heat transfer in the considered non-uniform channel is very similar to that in a buoyancy aided pipe flow. Heat transfer is impaired by the buoyancy force first, but recovers when the heat flux is sufficiently high. The turning point of the trend is largely the same as that in a buoyancy-aided pipe flow. However the heat deterioration due to buoyancy force is weaker than in the pipe flow. This is due to the non-uniform buoyancy effect on turbulence in the geometry considered herein.

KEY WORDS
Turbulence, Nuclear energy, Instability, Buoyancy

1 INTRODUCTION

Rod bundles are typical design features of the fuel assemblies in many nuclear reactors. The coolant flows through the sub-channels formed by arrays of fuel rods (or pins). Such sub-channels are connected to each other through 'narrow' gaps of continuously varying sizes, which are characterised by the non-dimensional pitch-to diameter ratio. Such non-uniform cross-sections of flow passage can potentially cause the formation of large unsteady coherent structures, which enhance flow mixing and hence the cooling of the fuel rods. They could also lead to structural vibrations causing, for example, grid-to-rod fretting in Pressurised Water-cooled Reactors (PWRs).

The unsteady flow structures have been investigated in many experiments. Hopper and Rehme carried out an experimental study on the developed turbulent flow through closely-spaced rod arrays in 1984 [1]. The pitch to diameter ratio *P/D* and the distance-to-wall to diameter ratio w/d were 1.036 and 1.072, respectively. The results of the experiments showed that an energetic azimuthal turbulent-velocity component and large-scale semi-periodic structures exist in the narrow gaps between the rods. Rehme [2] and Meyer [3] independently linked such quasi-periodic flow pulsations to the high mixing rates between the subchannels of the rod bundles observed in their experiments. Meyer found that the characteristic frequency of the flow pulsation depends on the rod bundle geometry and the flow velocity [3]. In later experiments carried out by Kraus and Meyer [4] on the triangular arrays with pitch-to-diameter ratio *P/D=1.12* and *P/D=1.06*, the existence of large-scale periodic fluctuations of velocity and temperature in the gap regions was revealed. They concluded that such fluctuations were responsible for the high inter-subchannel heat and momentum exchange which was further proved by another experiment done by them in 1998 [5]. Wu and Tupp [6] did an experimental study on the turbulence intensity in rod-to-wall gap regions formed by a rod mounted in a

*Corresponding author

trapezoidal duct [6]. The ratio between the height of the narrowest gap and the rod diameter was *H/D*=0.08.They observed high turbulence kinetic energy and turbulence intensity in the narrow gap. The high turbulence kinetic energy disappeared when the gap size was extremely small. They claimed that the flow pulsation in the narrow gap is the reason for such abnormal turbulence behavior in the narrow gap between rod and wall. Guellouz and Tavoularis [7, 8] visualized the large-scale quasi-periodic structures in the gaps of various sizes. They described such structures as a street of three-dimensional, counter-rotating vortices [7, 8]. The frequency of pulsations was found to decrease with diminishing rod–wall gap size in certain ranges; meanwhile, the pulsations in a rod–wall gap and an adjacent rod–rod gap were strongly coupled [9]. Furthermore such flow pulsations can exist even in a laminar flow [10, 11].

Chang and Tavoularis [12] carried out a numerical simulation of the axial flow in a rectangular channel containing a cylindrical rod with *H/D=0.1*, which is similar to that of Guellouz and Tavoularis [7, 8]'s previous experiments [7, 8]. The unsteady Reynolds-averaged Navier-Stokes equations with a Reynolds stress model were solved using the commercial CFD software package Ansys Fluent. The results, such as, mean velocity and Reynolds stresses distributions, agreed fairly well with previous experiments. Furthermore, pairs of large-scale, quasi-periodic, vertical coherent structures were clearly shown at each side of the gaps. The same method has been employed to study flow in a section of the 37-rod bundle of the fuel assembly of the CANDU nuclear reactors [13]. The results were in good agreement with experiments. They showed that the velocity fluctuations at different locations were strongly correlated with each other. In another numerical study, the impact of the size of the gap between the rod and the rectangular walls was investigated [14]. They demonstrated that the turbulent kinetic energy and temperature fluctuations increase with the decrease of the gap size from 0.1D to 0.03D. However, the fluctuations disappear when the gap size decrease to 0.01D. Furthermore, they carried out an investigation on the validation of different turbulence models in the predication of such flow structures [15]. They found that large eddy simulation (LES) is the most accurate method, while the unsteady Reynolds-averaged Navier-Stokes equations with Reynolds stress model is also an acceptable choice. The latter can produce reasonable results with much lower computational cost. Ninokata et. al.[16] and Merizari and Ninokata [17] simulated the flow in an eccentric annular channel using Direct Numerical simulation (DNS) and large eddy simulation(LES) with dynamic Smagorinsky subgrid-scale model. The large-scale oscillations were found around the narrow gaps. They play an important role in transporting turbulence from wider regions to the narrow gaps. Furthermore, such oscillations become less significant with the increase of the Reynolds number. The results of the LES were found to be as accurate as those of the DNS. In their further study on the flow in tight lattice rod-bundles [18], the existence of large-scale periodic flow oscillations has been shown as well. They linked this phenomenon to the interactions between coherent structures in adjacent sub-channels. Yan, et al. [19] introduced heat transfer into the study of the coherent structures in tight lattice. They again proved that coherent structures exist in a wide range of Reynolds numbers in tight lattices, and the gap size is the most critical factor. However the effect of the coherent structures on heat transfer was not discussed.

Most of the studies that have been conducted to date on the flow structures in the gap flow are based on isothermal flows, but in the real world heat transfer is present in the rod bundles in the nuclear reactors. In addition, it is reasonable to expect that under certain conditions buoyancy forces can significantly affect the flow in the rod bundles. The current study focuses on the effect of the buoyancy force on the large flow structures in the gap regions and heat transfer in a sub-channel formed by a trapezoidal enclosure surrounding a circular rod (Figure 1).

2 COMPUTATIONAL DOMAIN AND NUMERICAL PROCEDURES

2.1 Computational Domain

The geometry of the flow cross-section in the current study is the same as that used in the experiment by Wu and Trupp [6]. It is formed from a trapezoidal channel enclosing a rod in it as shown in Figure 1. The flow passage is bounded by the rod and trapezoid wall. The diameter of the rod is d= 50.8mm, and the height of the trapezoid wall is 66.0mm. The lengths of the short and long edges of the trapezoid are 50.8mm and 127.0 mm, respectively. The height of the narrow gap g = 4mm, whereas the height from the top of rod to the long edge of the trapezoid bound (s) is 54.8mm, which gives the wall to diameter ratio s/d= 1.08. The hydraulic diameter of the channel D_h=31.4mm. The total length of the computational domain is $10D_h$. The *X*-direction is named as the spanwise direction, Y-direction is the transverse direction, and Z-direction is the streamwise direction.

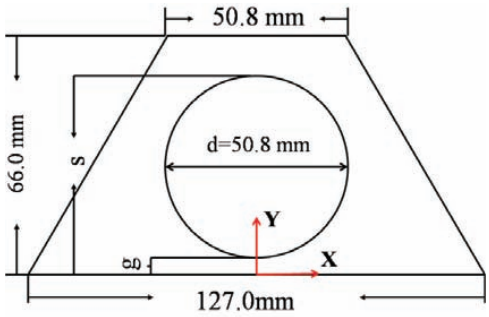

Figure 1 Schematic of the trapezoid-bounded subchannel cross section.

2.2 Computational Procedure

Numerical methodology. Large-eddy simulation (LES) and energy equations implanted in Fluent 14.5 are adopted to simulate incompressible, 3-dimensional flow and mixed convection heat transfer in the channel. The subgrid scale viscosity is modelled by using the wall-adapting local eddy-viscosity (WALE) model. By describing the subgird scale viscosity as a function of the strain and rotation rates, the WALE model has been shown to perform well in shear flows, which makes it suitable for complex geometries. Furthermore, the subgrid viscosity naturally goes to zero at wall in WALE, as demonstrated in the article by Nicoud and Ducros [20]. It allows the subgrid scale (SGS) viscosity to be damped in the near wall region as dynamic models, but more stable than then ,because WALE model always generate positive SGS viscosity, while negative values can be generated by dynamic models.

Simulation cases. Four cases have been studied to investigate the performance of buoyancy-aided flow in the channel with various buoyancy forces. The first One is a forced convection flow case omitting the buoyancy completely (referred to as 'Case 1'), while the other cases include the buoyancy force, and are hence mixed convection or buoyancy-influenced cases (referred to as 'Case 2', 'Case 3' and 'Case 4'). The Boussuniesq approximation is utilized to simulate the buoyancy force in these cases. The properties of the fluid are the same in all the cases.

Properties and boundary conditions. An air-like fluid is chosen as the working fluids. The density, specific heat, thermal conductivity, and viscosity are 1.225 kg/m^3, 1006.42 j/kg·K, 0.0242 w/m·K and 1.7894e^{-5} kg/m·s, respectively in the cases. To activate the buoyancy force, the thermal expansion coefficient is set as 0.001 K^{-1} in all of the buoyancy influenced cases. Both side walls and the tube wall are heated in these three cases. The temperatures of all the walls are set to be the same constant, being 800K, 650K 1427K and 6250K in Cases 1, 2, 3 & 4, respectively. The bulk fluid temperatures of incoming flow in the cases at the inlet are 350K, 300K, 700K and 3000K, respectively. Hence, the buoyancy parameter Bo^* is $1.5x10^{-6}$, $2.4x10^{-6}$ and $1.7x10^{-5}$ for the latter three cases respectively. The periodic boundary condition is applied to both the flow and thermal fields in the flow direction (namely at the inlet and outlet) to simulate a fully developed flow. The mass flow rate is 0.011522 kg/s, making the Reynolds number approximately 5270. The gravity acceleration is 9.8m/s and opposite to the flow direction in Cases 2, 3 & 4.

Mesh and numerical methods. Since the flow in the near wall region is resolved by the LES, a relatively fine mesh is required. A mesh with non-uniform element size has been generated. The grid size is small in the near wall region but bigger in the main channel. The first near wall mesh resolutions, calculated in Case 1, are in the ranges of $5 \leq \Delta x^+ \leq 17$, $0.13 \leq y^+ \leq 0.2$ and $10 \leq \Delta z^+ \leq 16$. There are at least 15 cells located between the wall and $y^+ = 20$. An overview can be seen in Figure 2. There are about 30,000 cell elements in a radial-circumferential cross section. Vertically, there are 257 divisions. The whole computation domain contains 7.74 M elements in total. The filtered Navier-Stokes equations and the energy equation are discretized by the bounded central differencing scheme and the second order upwind scheme respectively. The SIMPLE scheme is used for the coupling of the pressure and velocity. The time step, Δt is 0.0001s,

corresponding to a CFL (Courant-Friedrichs-Lewy) number $U_b\Delta t/\Delta z$ of 0.2, where U_b is the averaged bulk velocity.

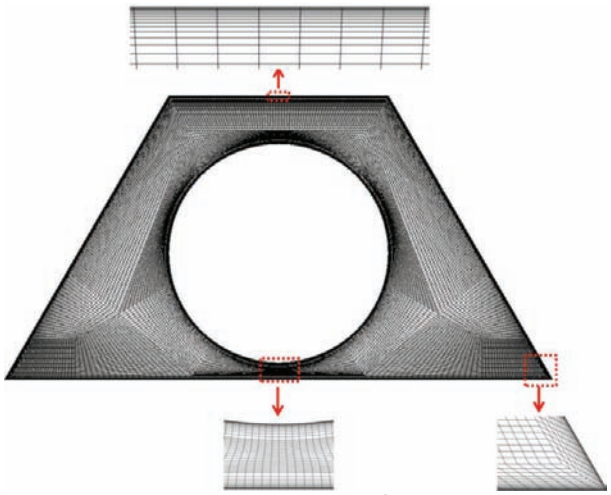

Figure 2 The overview of the mesh.

3 RESULTS ANDDISCUSSIONS

Several lines and surfaces located in the flow domain have been selected to show the instantaneous flow pattern and to form the basis for statistics analysis, referring to Figure 3. The turbulent velocity histories and the power spectra densities at points 'MP1' and 'MD' are shown in section 3.1. The flow statistics along 'P1', 'P2' & 'P3' and 'ML1', 'ML2' & 'ML3' are presented in the section 3.3.

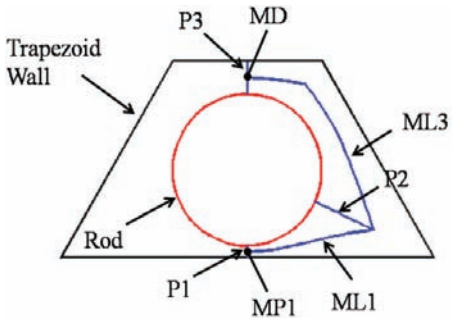

Figure 3 Locations used in results discussion.

3.1 Flow Pattern

Instantaneous velocity. Normalised fluctuating azimuthal velocity (u'/U_b) and streamwise velocity (w'/U_b) at 'MP1' and 'MD' are presented in Figures 4 and 5. It can be seen in Figure 4 (a), *u'* oscillates at the position MP1 in all of the cases. The amplitude is as high as ~35%U_b in Case 1, and decreases slightly in Case 2 (~25% U_b) and Case 3 (20% U_b), but recovers in Case 4. The period of *u'* is not perfectly constant in all of the cases. As shown in Figure 4 (b), very weak oscillations of *u'* with the strong turbulent noise contamination are also observed at 'MD' in Case 1, while they are effectively vanished in Case 2, but are strengthened in Cases 3 & 4. It is interesting to note that the dominant periods of *u'* at 'MD' in Cases 3 & 4 are very close to each other, whereas those at 'MP1' are very different. Similar to u'/U_b, the quasi-periodic oscillations also exist in the history of w'/U_b at 'MP1' in the cases, see Figure 5(a). The dominant periods of

w'/U_b at MP1 in the cases are about a half of that of u'/U_b, except for Case 4. In Case 4 such period is more or less that same as that of u'/U_b. These results suggest that flow in the vicinity of the narrow gap swing from left to right and left to right periodically in Cases 1, 2 & 3, but not in Case 4. As shown in Figure 5 (b), no obvious regular oscillations are observed at 'MD' in Case 1 & 2, but some can be observed in Case 3 & 4, although the signal in Case 4 is heavily affected by turbulence noises. The dominant frequency of w' is revealed later using power spectra density..

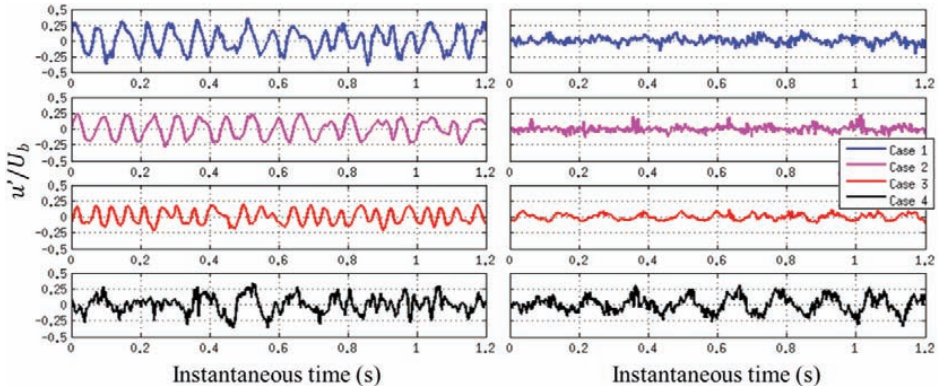

(a) (b)

Figure 4 The history of spanwise turbulence velocity u' (normalized by bulk velocity U_b) in (a) the narrower gap ('MP1'); and (b) the wider gap ('MD') in all of the cases.

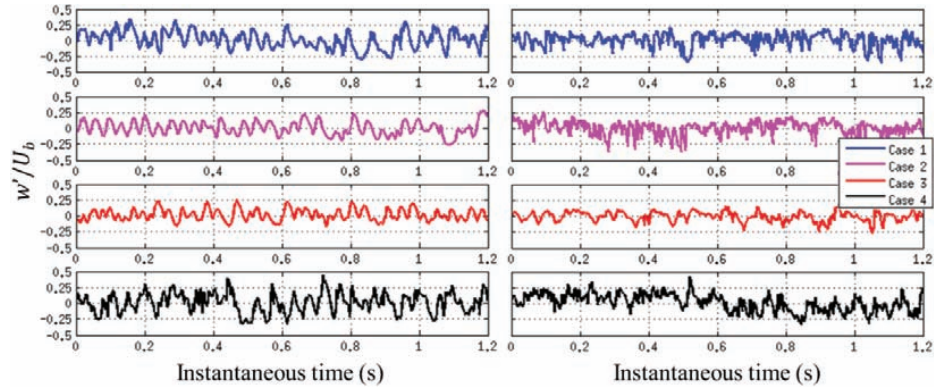

(a) (b)

Figure 5 The history of streamwise turbulence velocity w' (normalized by bulk velocity U_b) at (a) 'MP1' and (b) 'MD' in all of cases.

Power spectra density. To exactly determine the dominant frequency of the flow structures, it is useful to study the power spectra density of the instantaneous turbulent velocities at 'MP1' and 'MD', which are presented in Figure 6. The power spectra densities of *u'* and *w'* are denoted as PSDX and PSDZ in the following discussions. To make the results from different cases more distinguishable, the results from Cases 1, 2, 3 & 4 are multiplied by a factor of '10^0', '10^2', '10^4' and '10^6', respectively. Similar to the observation by Wu and Trupp [6], the peak in PSDX does not just exist in the narrow gap (referring to 'MP1'), but also at the centre of the big gap ('MD'), in all of the cases, see Figure 6 (a & b). Together with the behaviour of *u'* at both locations in the cases, it is reasonable to conclude that there are also big flow structures existing in the big gap. The presence of secondary peaks located at both sides of the dominant peak, in the cases except in Case 4, suggests that coherent flow structures in the narrow gap co-exist with other structures in the channel. Furthermore, there is a secondary peak located at the left of the dominant peak at 'MP1', with its frequency very similar to the dominant frequency of PSDX at 'MD', in Cases 1, 2 & 3, which suggests that the influence of the structures passing the big gap can reach to the narrow gap of the channel. Meanwhile,

the fact that the frequencies of PSDX at 'MP1' and 'MD' in Case 4 are similar implies that the structures in the narrow gap and big gap are strongly correlated with each other.

Regarding the PSDZ at 'MP1', see Figure 6 (c), the peak is much weaker than its counterpart in PSDX. The figure clearly shows that the peak frequency in PSDX is nearly doubled that in PSDX in Cases 1 and 2, while the pronounced peak disappears in Case 3. The value of the dominant frequency in PSDZ at 'MP1' in Case 4 is very similar to its counterpart in PSDX. The double peaks of the frequency of PSDZ at 'MP1' in Cases 1 & 2 are because the axial velocity changes twice with the flow oscillating for a full cycle in the narrow gap. In contrast to the absence of spikes in PSDZ at 'MD' in Cases 1 & 2, there are visible peaks in PSDZ at 'MD' in Cases 3 & 4, as illustrated in Figure 6 (d). In addition, the peak frequency of PSDZ at 'MD' in Cases 3 and 4 is similar to that in PSDX at the same location. This again implies that the structures passing 'MD' is different from the dominant structures in the narrow gap.

Consistent with findings from previous studies, the dominant frequency of the flow structure in narrow gap depends on the geometry and flow velocity. It has also been found previously that the non-dimensional frequency Strouhal number (St_τ), defined as fD_h/u_τ (where f is the dominant frequency, D_h is the hydraulic diameter and u_τ is the friction velocity) is dependent only on the geometry configuration. In the current simulation the St_τ^{-1} evaluated in Case 1 is 0.3787, which is about doubled the value 0.16 in Wu and Trupp [6]. However the St_{Ub}^{-1} $(= fD_h/U_b)$ evaluated by using the bulk velocity is 5.57, which is very close to the experimental results 5.20. The non-linear relationship between friction velocity and Re number can be the reason. This result suggests that the St is better correlated with U_b not friction velocity. To avoid confusion, the St mentioned below is evaluated using bulk velocity. The relationship between St^{-1}/St_f^{-1} and buoyancy parameter Bo^* is shown in Figure 7. St is the Strouhal number in buoyancy influenced cases and St_f is from Case 1. A negative relationship between St^{-1} and Bo^* is established when the buoyancy force is small, see the values of St^{-1}/St_f^{-1} in Case 2 & 3. But St^{-1}increases with the increase of the buoyancy force as $Bo^*$is beyond certain value. Meanwhile, it also can be seen from the figure that St^{-1} in the big gap follows the same trend, but the response of St^{-1} to the change of Bo^* is much moderate.

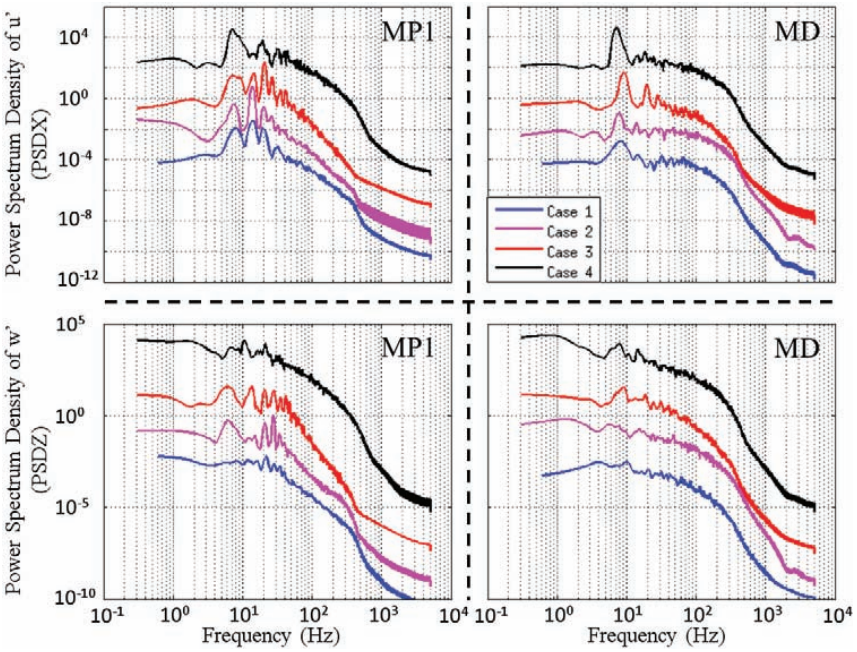

Figure 6 Power spectral density of the u'(PSDX) and w' (PSDZ) at 'MP1' and 'MD' in all of cases. To make results more distinguishable, original results from Cases 2, 3 and 4 are multiplied by the factor 10^2, 10^4 and 10^6, respectively.

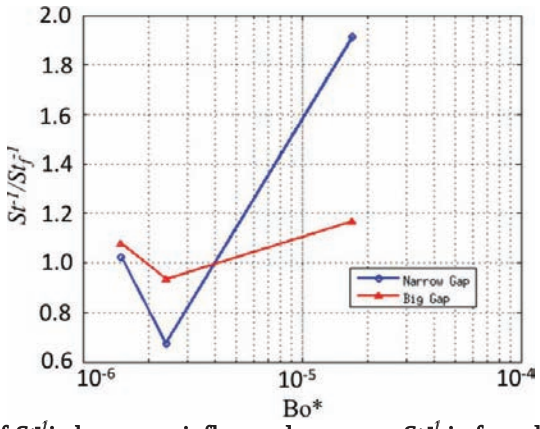

Figure 7 Ratio of St^{-1} in buoyancy influenced case over St_f^{-1} in forced convection case.

3.2 Heat Transfer

In spite of the enormous amount of heat transfer data on the mixing convection in vertical pipes or channels, the knowledge on channels similar to the current geometry configuration is still limited. The influence of the buoyancy force on the heat transfer of mixed convection in the current channel is compared to the mixed convection in a pipe. The DNS data credited to You et al. [21] and results obtained using Launder-Shamer model by Kim et al. [22] have been chosen here for this purpose. The You et al. [21]'s DNS was devoted to investigating the fully developed turbulent mixed convection due to air flowing upwards in a vertical pipe with a Re number of 5300. The work done by Kim et al. [22] was to investigate the performance of different models on predicting the mixed convection under conditions as reported in You et al. (2003). Again, buoyancy aided flow was considered, which is the same as the current investigation.

To obtain a general picture of the forced and mixed convection heat transfer, the Nusselt number (*Nu*) of the considered cases and results of the forced convection case reported by You et al. [21] have been show in Figure 8 (a), and the effect of buoyancy force on Nu of current geometry configuration and pipe (You et al. [21] and Kim et al. [22]) are shown in Figure 8 (b).

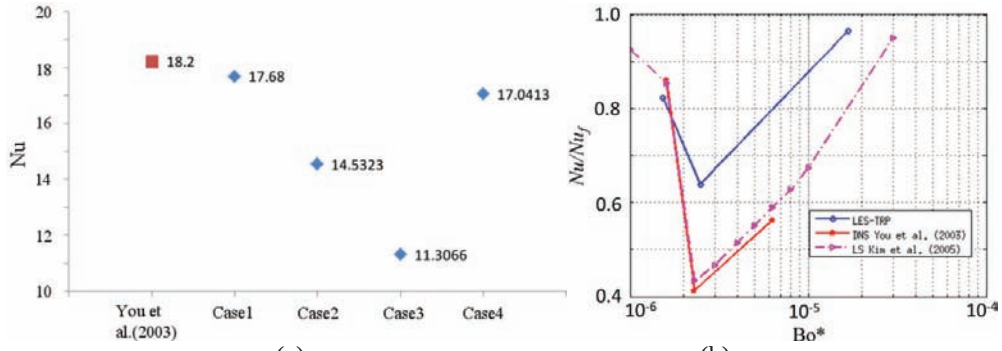

(a) (b)

Figure 8 (a)Nu of the current simulation Cases; (b)Influent of buoyancy on heat transfer in buoyancy cases and references simulations.

The *Nu* of forced convection in the current geometry is very similar to DNS result of a heated pipe. The difference between the values in the two geometries is just 0.52 (~2.86%), refer to Figure 8(a). It also shows that *Nu* firstly decreases with the increase of the buoyancy force. It increases again when the heat flux is sufficiently high. Such a trend is the same as the buoyancy aided pipe flow. However, the significance of buoyancy effect on the mixed convection in these two geometries is different. As shown in Figure 8(b),

Nu/Nu_f in the present cases is slightly smaller than that of pipe for $Bo^* \cong 1.6 \times 10^{-6}$, Case 2, while Nu/Nu_f is generally much higher than the values of the heat flow in the pipe under the buoyancy aiding condition as $Bo^* > 2 \times 10^{-6}$. The value of the buoyancy parameter at which the strongest heat transfer deterioration occurs is more or less the same in two types of channels.

3.3 Statistics Analysis

Mean flow. The contours of the axial velocity distribution in the cases are shown in Figure 9. As expected, the high velocity patch is located in the main channel in the forced convection case. The velocity decreases as the flow passage becomes narrower. Such velocity distribution is modified as the buoyancy force is introduced into the system. For example, the high velocity patch is moved to the top corner and spreads to the big gap in Case 2. With further increase of the buoyancy force, the high velocity patch also extends towards the main channel; see the velocity contour of Case 3. When the buoyancy force is sufficiently high, the velocity in the bottom narrow gap and the corners is greatly accelerated; as demonstrated in Case 4.

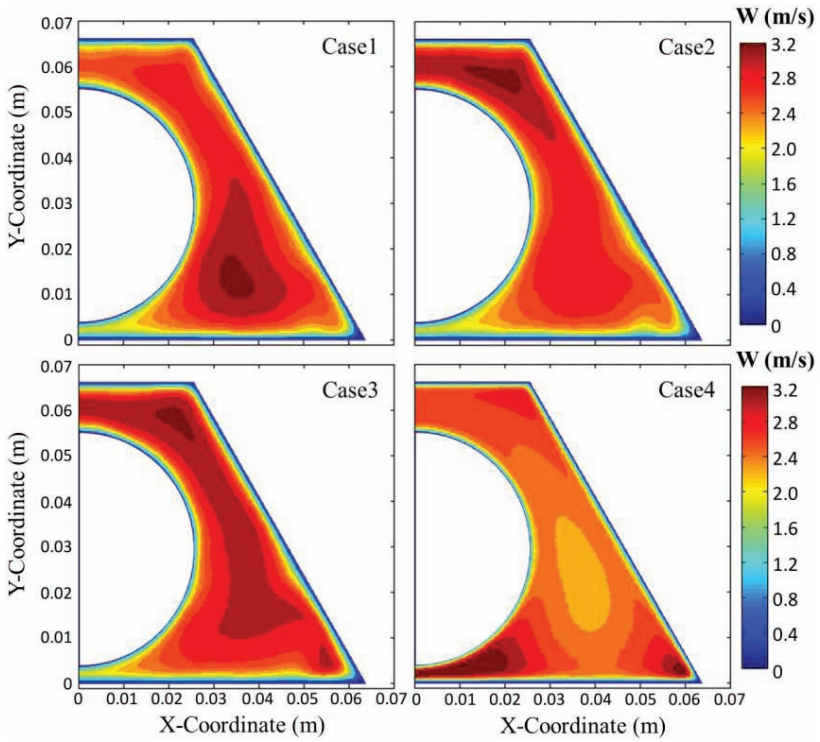

Figure 9 Contours of streamwise velocity W (m/s).

More details can be seen from the velocity profile along the pre-defined lines ('ML1', 'ML2', 'ML3' and 'P1', 'P2', 'P3'), see Figure 10 (a). Considering the velocity distribution on the equal-distance lines ('ML1', 'ML2' and 'ML3') in Case 1, the velocity increases gradually from the centre of the narrow gap, reaches the first peak in the main channel, after which it starts to decrease until the location in the next relatively bigger opening of the channel (the end of 'ML2'), the velocity decreases again after that with the location moving to the centre of big gap. The shape of the velocity distribution along 'ML1' is similar in Cases 2 and 3. The velocity continues decreasing along 'ML2' albeit in a much slower rate. The velocity along 'ML3' in these two cases decreases with the location moving to the centre of narrow gap, but with a rate that is much smaller than that in Case 1. The picture is completely different in Case 4. As shown in the figure, the maximum velocity is located at the vicinity of the narrow gap. Then, the velocity decreases until the channel starts narrow up again, referring to 0.06m in Figure 10(a). The velocity increases beyond this point, until it reaches a flat level along 'ML3'. A very uniform velocity distribution can be found along the centreline of the narrow gap.

The velocity distributions on 'P1', 'P2' and 'P3', shown in Figure 10 (b, c, & d), from all of the cases are shown here to further the understanding on the influence of buoyancy force on local velocity profile. Due to the non-uniformity of the flow passage, the flow behaviour is different in different regions of the channel, such as the narrow gap, main channel and big gap. In Case 1, the flow in the narrow gap is similar to laminar flow and a parabolic velocity profile can be observed on 'P1'. The flow is clearly turbulent in the main channel, as can be seen from the shape of the velocity profile on 'P2'. The velocity profile on 'P3' again exhibits a turbulent flow behaviour in the big gap. Moreover, the effects of body force on the velocity profile along the lines in the different regions are quite different. The velocity profiles on 'P1' in the first 3 cases almost overlap with each other, while it is higher greatly in Case 4, see Figure 10 (b). The shape of the velocity profile along 'P2' is again very similar to each other in the first three cases, while the velocity magnitude and gradient in the near wall region are slightly lower in Cases 2 & 3, due to the buoyancy force. In the meantime, the velocity magnitude is smaller than the value in Case 1 in the centre of the channel in these two cases. When the heat flux is sufficiently high as in Case 4, the velocity in the near wall region is recovered and a concavity developed in the velocity profile, see Figure 10(c). As shown in Figure 10(d), the velocity along 'P3' is overall higher in Cases 2 and 3, compared to the profile in Case 1. The velocity profile is turned into a 'M' shape in Case 4, which would result in regeneration of turbulence. In comparison with Case 1, the velocity gradient along 'P3' in the near wall region is firstly increased in Case 2, returns to the magnitude of Case 1 in Case 3, but is increased again in Case 4.

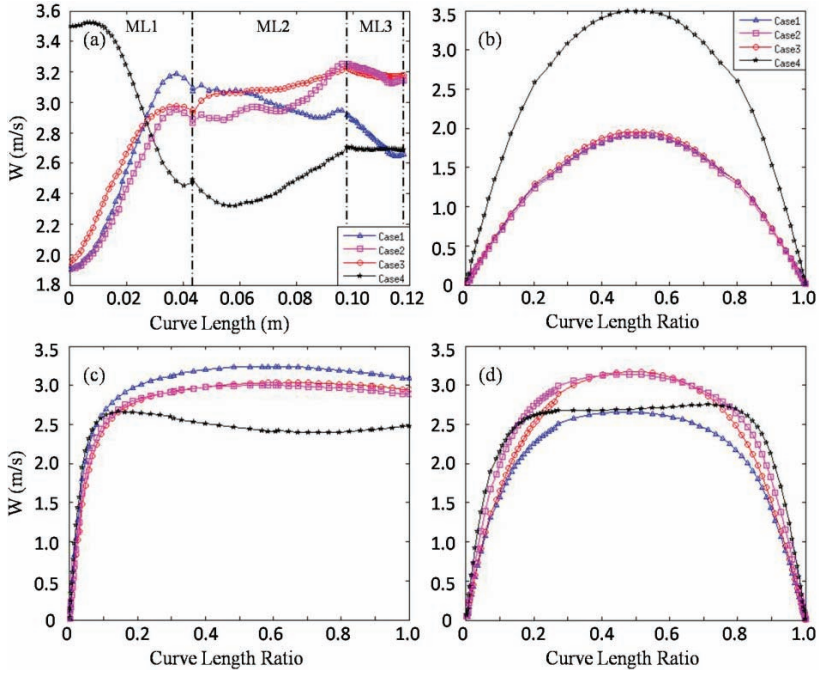

Figure 10 Averaged streamwise velocity *W* (m/s) along lines: (a) 'ML*' (b) 'P1'; (c) 'P2'; (d) 'P3'.

Turbulence kinetic energy. The contour of the turbulence kinetic energy (*k*) and the profile of it on the predefined lines mentioned above ('ML'* and ' P*') are shown in Figures 11 & 12, respectively. It can be seen in Figure 11 that there is a high turbulence kinetic energy region, which is located in the vicinity of the narrow gap in Case 1. This is similar to that found in the experimental work by Wu and Trupp [6]. The magnitude of such high turbulence kinetic energy is reduced in Cases 2 and 3. It can be explained by the *laminarization effect* due to buoyancy force. With a further increase in the buoyancy force, turbulence is regenerated, which can be detected from the contour of k/U_b^2 in Case 4. It is also interesting to note that the size of the high turbulence region in the near gap region in Case 4 is much bigger than in other three Cases. In the meantime, the high turbulent patch in the near wall region is disappeared, while a general increase of

turbulence kinetic energy level in the core region of the whole channel can be seen from the contour of k/U_b^2 in Case 4.

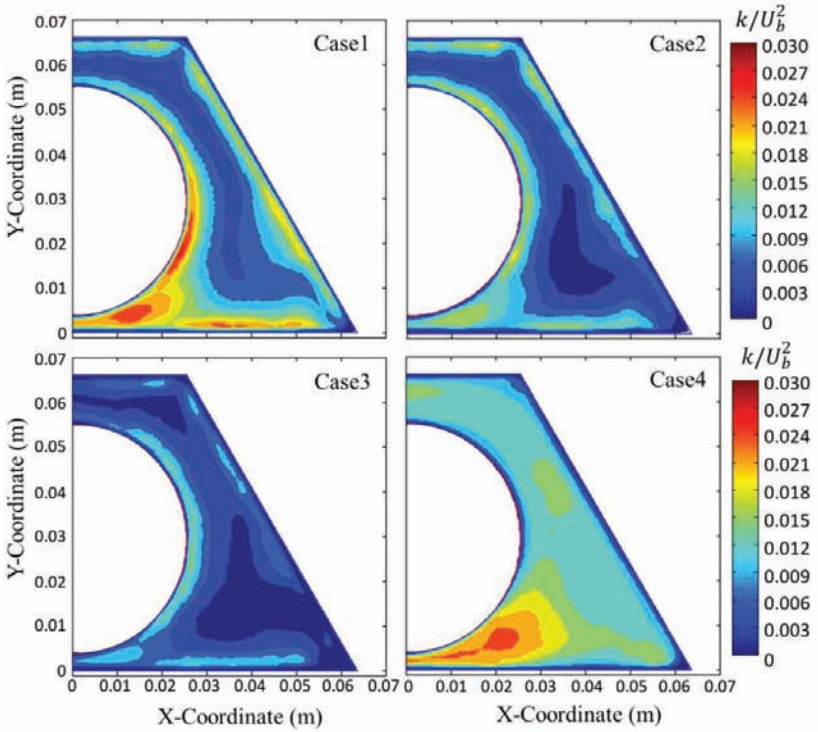

Figure 11 Contour plot of turbulence kinetic energy (k/U_b^2) in four cases.

The profiles of k/U_b^2 along the 'ML*' (refers to 'ML1', 'ML2' and 'ML3'), 'P1', 'P2', and 'P3' are illustrated in Figure 12. As shown in figure, the peak of k/U_b^2 along 'ML1' in Case 2 is 70% of that in Case 1, which further drops to 50% in Case 3. The value of *k* along 'ML2' and 'ML3' is generally smaller in Cases 2 and 3, but the reduction is smaller compared to the value on 'ML1'. While the turbulent kinetic energy on 'ML1' recovers in Case 4, it is almost tripled on 'ML2' and 'ML3' compared to the value obtained in Case 1. The same trend can be seen from the distribution of k/U_b^2 on 'P1': Turbulence reduction occurs in Case 2 and 3, but it recovers in Case 4. The reduction of *k* in the near wall region along 'P2' occurs in all of the buoyancy influenced cases. The values of k/U_b^2 on 'P2' reduce with the increase of buoyancy force in Cases 2 & 3, while the peak of *k*in Case 4 is similar to that in Case 2 and the location of the peak moves away from the near wall region. Meanwhile, the value of k/U_b^2 in Case 4 is more than tripled that that in Case 1 in the core region. The location of that of k/U_b^2peak on P3 in Cases 1, 2 & 3 is closer to the wall than in Case 4. Interestingly,k/U_b^2 in the vicinity of the wall in Case 2 is increased but is significantly decreased in Case 3. The peak value of k/U_b^2 in Case 4 is similar to that in Case 2. Again a high turbulent kinetic energy can be found in the centre of the big gap in Case 4.

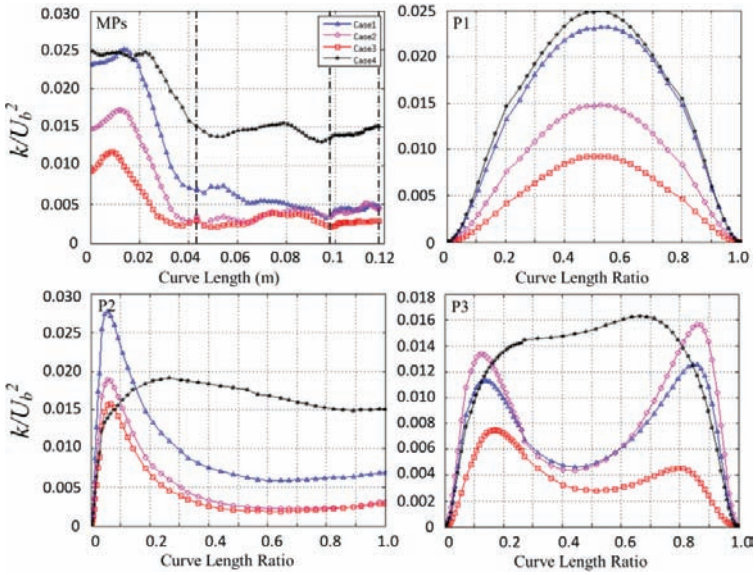

Figure 12 turbulent kinetic energy (k/U_b^2) on 'ML*', 'P1', 'P2' and 'P3'.

Turbulence production. As shown above, high turbulent quantities are mainly located on the 'ML1'. Reynolds stresses production terms of the kinetic energy along 'ML1', 'P1', 'P2' and 'P3' are shown in Figure 13. A peak of the turbulence production on 'ML1' can be found in all of the cases. The peak value is greatest in Case 1, while it decreases with the increase of buoyancy force in the other 3 cases. Meanwhile, the location of the peak on 'ML1' moves towards the narrow gap centre in Case 2 and Case 3, but moves away from it in Case 4. Overall the reduction of the peak value can be more than 50% in the buoyancy influenced cases. The weakest peak is in Case 4, although that the peak values of only slightly higher than in cases 2 & 3. This trend remains in the distribution of turbulent production rate along 'P2', but not along 'P1' and 'P3'. The turbulence kinetic energy productions mainly occur in the near wall region along all the three lines, 'P1', 'P2' & 'P3'. On 'P1', the most significant peak value (~4.8 m^2/s^3) is found in Case 4, which is almost double the value (~2.4 m^2/s^3) in Case 1, while the value can be less than 0.8(m^2/s^3) in Case 2 and around 0.3 (m2/s3) in Case 3. The highest value of the peak (~7m^2/s^3) of turbulence production on P3 is found in Case 2, the lowest (~2m^2/s^3) again found in Case 3, while (~5.4m^2/s3) and (~2.8m^2/s^3) in Case 1 and Case 4, respectively.

The buoyancy production of the turbulence kinetic energy on selected lines is shown in Figure 14. Since g = 0 m/s^2 in Case 1 the buoyancy production term in Case 1 is 0 m^2/s^3. Generally speaking, the body force plays a negative role in Cases 2 & 3. The locations of the minimum values on 'ML1' are similar to that of the peak of $\langle w' \rangle / U_b$ on each selected lines in these two cases and the negative value is more significant in Case 3. Such negative effect is stronger in Case 3. A strong and positive buoyancy production can be found in Case 4. The value in Case 4 increases from the centre of narrow gap and reaches a peak at a location where the highest *k* located. The peak value is the same as that of the production due to the Reynolds stresses. Again a positive buoyancy production can be found on 'P1' in Case 4, especially in the centre of narrow gap, while a negative production (i.e. a sink) can be found in Cases 2 and 3. Although a negative production can be found in Case 4 in the near wall region on 'P2' and 'P3', a significant positive buoyancy production can be found in the region far from the wall. However, the value is mainly negative on 'P2' and 'P3' in Cases 2 and 3, especially in the near wall region.

Overall, turbulence is reduced with the increased of heat transfer when $Bo^* < Bo_0^*$, and recovers when the heat flux is further increased so that $Bo^* > Bo_0^*$. When $Bo^* < Bo_0^*$, the buoyancy force does not just decrease the magnitude of the turbulence production by modifying the shear stress, but also plays a negative role in the turbulence production due to the negative value of the buoyancy production. When the heat flux is sufficiently high, the buoyancy production is very high in the region away from the wall, which results a high turbulence regenerate in the core region, even though the shear production term is smaller than in the

forced convection case. The strength of the buoyancy effect on turbulence in the non-uniform flow passage is location dependent. Under particular thermal boundary conditions, turbulence can be locally enhanced at certain regions while it is suppressed by the body force in other places. Because of this, the laminarization effect of buoyancy flow is much weaker in the non-uniformly channel, which results in a more gentle heat transfer impairment compared to that in a tube at the same Bo^*.

The existence of the vortex in the vicinity of the narrow gap in the forced convection case results in more turbulence generated in the narrow gap. Such an effect is reduced by the buoyancy force when $Bo^* < Bo_0^*$, although the form of the large flow structure is not changed much by the buoyancy force. The reduction is not just due to the decreased shear production but the negative buoyancy production. Due to the strong positive buoyancy production, turbulence in the region can be as high as that in the forced convection case.

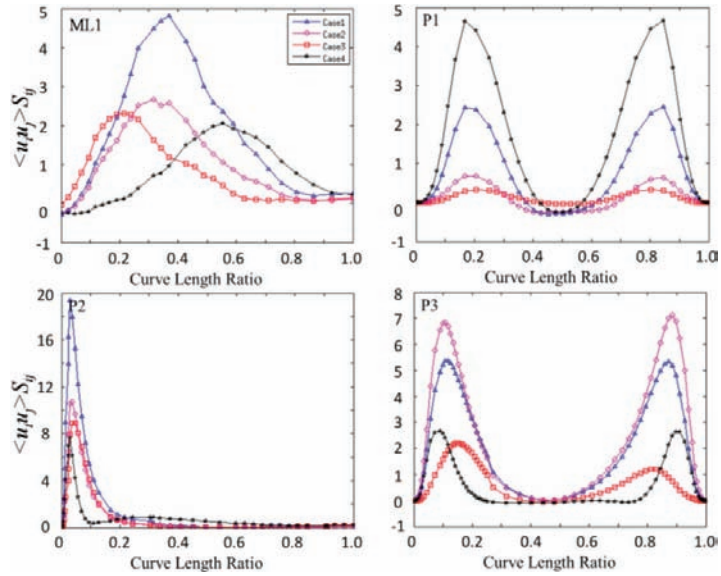

Figure 13 The shear stress production of the turbulence kinetic energy.

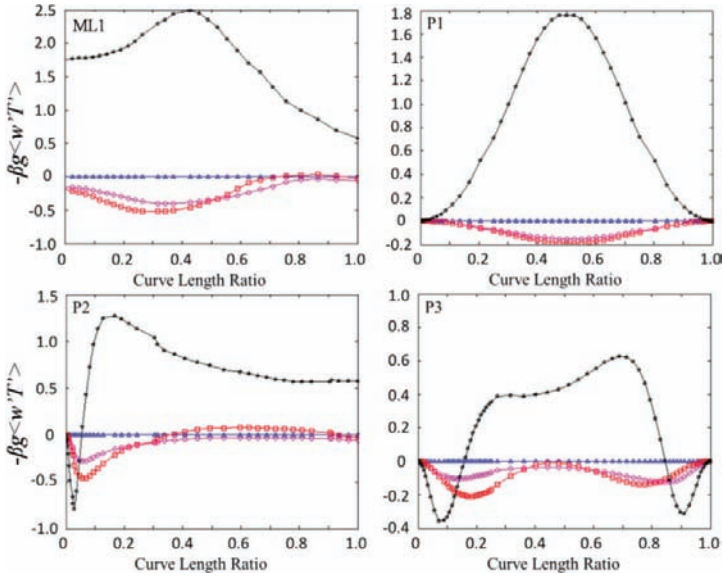

Figure 14 Gravity production of the turbulent kinetic energy.

4 CONCLUSIONS

Large eddy simulation with the WALE model is utilized to investigate the buoyancy-aid flow in the rod to gap regions. Four cases with various thermal boundary conditions are considered. It is found that oscillatory flow structures exist in the vicinity of narrow gap for cases with buoyancy parameter Bo^* is smaller than the critical value Bo_0^*, where the strongest heat deterioration occurs. With a further increase of heat flux (as $Bo^* > Bo_0^*$), the characteristic of the flow structure changes. The coherent flow structures in the narrow gap can be strongly affected by flow structures in other part of the channel, including the flow structure passing the top big gap. The structures in the narrow and wider gaps are strongly correlated with each other when the buoyancy force is strong.

Under the forced convection conditions, the Nu number of the flow in the considered channel is very similar to that obtained in a tube. The effect of buoyancy force on the heat transfer in the geometry considered here is qualitatively similar to that in a tube flow, but the heat transfer impairment is weaker in the non-uniform geometry considered here. The critical buoyancy parameter Bo_0^* is very similar to the value obtained for a tube, although the Nu is ~50% higher than in that in the tube at the point. The non-uniformly distributed buoyancy effect on turbulence generation can be one of the reasons for such discrepancies. Also, the existence of large flow structures enhances the mixing, and hence improving the heat transfer in the narrow gap region.

REFERENCES

1. Hopper, J.D. and Rehme, K., "Large-scale structural effects in developed turbulent flow through closely-spaced rod arrays", *J. Fluid Mech.***145**, pp. 305-337, (1984).
2. Rehme, K., "The structure of turbulence in rod bundle and the implicatios on natural mixing between the subchannels", *Int. J. Heat Mass Transf.***35**(2), pp.567-581, (1992).
3. Moller, S.V., "Single-phase turbulence mixing in the rod bundles", *Exp. Therm. Fluid Sci.***5**, PP. 26-33, (1992).
4. Krauss, T. and Meyer, L., "Characteristics of turbulent velocity and temperature in a wall channel of a heated rod bundle", *Exp. Therm. Fluid Sci.***12**, pp. 75-86, (1996).
5. Krauss, T. and Meyer, L., "Experimental investigation of turbulent transport of momentum and energy in a heated rod bundle", *Nucl. Eng.Des.***180**, PP. 185-206 (1998).
6. Wu, X., Trupp, A.C., "Experimental study on the unusual intensity distribution in rod-to-wall gap region", *Exp. Therm. Fluid Sci.***6**, PP. 360-370, (1993).
7. Guelloz, M.S. and Tavoularis, S., " The structure of turbulent flow in a rectangular channel containing a cylindrical rod - Part 1: Reynolds-averaged measurements", *Nucl. Eng. Des.***23**, PP. 59-73 (2000).
8. Guelloz, M.S. and Tavoularis, S., " The structure of turbulent flow in a rectangular channel containing a cylindrical rod - Part 2: phase-averaged measurements", *Nucl. Eng. Des.***23**, PP. 75-91 (2000).
9. Baratto, F., Bailey, S.C.C., and Tavoularis, S., "Measurement of frequencies and spatial correlations of coherent structures in rod bundle flows", *Nucl. Eng. Des.***236**, PP. 1830-1837 (2006).
10. Gosset, A. and Tavoularis, S. "Laminar flow instability in a rectangular channel with a cylindrical core", *Phys. Fluids***18**(4), 044108, (2006).
11. Piot, E. and Tavoularis, S. "Gap instability of laminar flows in eccentric annular channels", *Nucl. Eng.Des.***241**, pp. 4615-4620,(2011).
12. Chang, D. and Tavoularis, S., "Unsteady numerical simulations of turbulence and coherent structures in axial flow near a narrow gap", *Trans. ASME***127**, pp. 458-466, (2005).
13. Chang, D. and Tavoularis, S., "Numerical simulation of turbulent flow in a 37-rod bundle", *Nucl. Eng. Des.***237**, pp. 575-590, (2007).
14. Chang, D. and Tavoularis, S., "Simulation of turbulence, heat transfer and mixing across narrow gaps between rod –bundle subchannels", *Nucl. Eng. Des.***238**, pp. 109-123, (2008).

15. Chang, D. and Tavoularis, S., “Numerical simulation of developing flow and vortex street in a rectangular channel with a cylindrical core”, *Nucl. Eng. Des.***243**, pp. 176-199, (2012).
16. Ninokata, H., Merzari, E., and Khakim, A., "Analysis of low Reynolds number turbulent flow phenomena in nuclear fuel pin subassemblies of tight lattice configuration", *Nucl. Eng. Des*.**239**, pp. 855-866, (2009).
17. Merzari, E. and Ninokata, H., "Anisotropic turbulence and coherent structures in eccentric annular channels", *Flow Turbulence Combust***82**, pp.93-120, (2009).
18. Merzari, E. and Ninokata, H., "Proper orthogonal decomposition of the flow in a tight lattice rod-bundle", *Nucl. Eng. Des.***241**, pp.4621-4632, (2011).
19. Yan B.H., Gu, H.Y. and Yu, L.,"Numerical simulation of coherent structure and turbulence mixing in tight lattice", *Progress in Nuclear Energy***54**, pp.81-95, (2012).
20. Nicoud, F. and Ducros, F., "Subgrid-Scale Stress Modelling Based on the Square ofthe Velocity Gradient Tensor", *Flow, Turbulence, and Combustion***62**(3), pp.183–200, (1999).
21. You, J., Yoo, JY. and Choi, H., "Direct Numerical Simulation of Heated Vertical Air Flows in Fully Developed Turbulent Mixed Convection", *Int. J. Heat Mass Transf*.**46**(9), pp 1613-1627, (2003).
22. Kim, W.S., He, S. and Jackson, J,D., "Assessment by Comparison with DNS Data of Turbulence Models Used in Simulations of Mixed Convection", *Int. J. Heat Mass Transf*.**51**(5-6), pp. 1293-1312, (2008).